Strange and multistrange particle production in Au + Au collisions at √sNN=62.4 GeV

(STAR Collaboration) Aggarwal, M. M.; ...; Planinić, Mirko; ...; Poljak, Nikola; ...; Zoulkarneeva, Y.

Journal article, Published version
Rad u časopisu, Objavljena verzija rada (izdavačev PDF)

Repository / Repozitorij:

Repository of the Faculty of Science - University of Zagreb

Strange and multistrange particle production in Au + Au collisions at $\sqrt{s_{NN}} = 62.4$ GeV

M. M. Aggarwal,[29] Z. Ahammed,[21] A. V. Alakhverdyants,[17] I. Alekseev,[15] J. Alford,[18] B. D. Anderson,[18] C. D. Anson,[27]
D. Arkhipkin,[2] G. S. Averichev,[17] J. Balewski,[22] D. R. Beavis,[2] R. Bellwied,[49] M. J. Betancourt,[22] R. R. Betts,[7] A. Bhasin,[16]
A. K. Bhati,[29] H. Bichsel,[48] J. Bielcik,[9] J. Bielcikova,[10] B. Biritz,[5] L. C. Bland,[2] W. Borowski,[40] J. Bouchet,[18] E. Braidot,[26]
A. V. Brandin,[25] A. Bridgeman,[1] S. G. Brovko,[4] E. Bruna,[51] S. Bueltmann,[28] I. Bunzarov,[17] T. P. Burton,[2] X. Z. Cai,[39]
H. Caines,[51] M. Calderón de la Barca Sánchez,[4] D. Cebra,[4] R. Cendejas,[5] M. C. Cervantes,[41] Z. Chajecki,[27] P. Chaloupka,[10]
S. Chattopadhyay,[46] H. F. Chen,[37] J. H. Chen,[39] J. Y. Chen,[50] J. Cheng,[43] M. Cherney,[8] A. Chikanian,[51] K. E. Choi,[33]
W. Christie,[2] P. Chung,[10] M. J. M. Codrington,[41] R. Corliss,[22] J. G. Cramer,[48] H. J. Crawford,[3] S. Dash,[12] A. Davila Leyva,[42]
L. C. De Silva,[49] R. R. Debbe,[2] T. G. Dedovich,[17] A. A. Derevschikov,[31] R. Derradi de Souza,[6] L. Didenko,[2] P. Djawotho,[41]
S. M. Dogra,[16] X. Dong,[21] J. L. Drachenberg,[41] J. E. Draper,[4] J. C. Dunlop,[2] M. R. Dutta Mazumdar,[46] L. G. Efimov,[17]
M. Elnimr,[49] J. Engelage,[3] G. Eppley,[35] M. Estienne,[40] L. Eun,[30] O. Evdokimov,[7] R. Fatemi,[19] J. Fedorisin,[17] R. G. Fersch,[19]
E. Finch,[51] V. Fine,[2] Y. Fisyak,[2] C. A. Gagliardi,[41] D. R. Gangadharan,[5] A. Geromitsos,[40] F. Geurts,[35] P. Ghosh,[46]
Y. N. Gorbunov,[8] A. Gordon,[2] O. Grebenyuk,[21] D. Grosnick,[45] S. M. Guertin,[5] A. Gupta,[16] W. Guryn,[2] B. Haag,[4] O. Hajkova,[9]
A. Hamed,[41] L-X. Han,[39] J. W. Harris,[51] J. P. Hays-Wehle,[22] M. Heinz,[51] S. Heppelmann,[30] A. Hirsch,[32] E. Hjort,[21]
G. W. Hoffmann,[42] D. J. Hofman,[7] B. Huang,[37] H. Z. Huang,[5] T. J. Humanic,[27] L. Huo,[41] G. Igo,[5] P. Jacobs,[21] W. W. Jacobs,[14]
C. Jena,[12] F. Jin,[39] J. Joseph,[18] E. G. Judd,[3] S. Kabana,[40] K. Kang,[43] J. Kapitan,[10] K. Kauder,[7] D. Keane,[18] A. Kechechyan,[17]
D. Kettler,[48] D. P. Kikola,[21] J. Kiryluk,[21] A. Kisiel,[47] V. Kizka,[17] S. R. Klein,[21] A. G. Knospe,[51] D. D. Koetke,[45] T. Kollegger,[11]
J. Konzer,[32] I. Koralt,[28] L. Koroleva,[15] W. Korsch,[19] L. Kotchenda,[25] V. Kouchpil,[10] P. Kravtsov,[25] K. Krueger,[1] M. Krus,[9]
L. Kumar,[18] P. Kurnadi,[5] M. A. C. Lamont,[2] J. M. Landgraf,[2] S. LaPointe,[49] J. Lauret,[2] A. Lebedev,[2] R. Lednicky,[17] J. H. Lee,[2]
W. Leight,[22] M. J. LeVine,[2] C. Li,[37] L. Li,[42] N. Li,[50] W. Li,[39] X. Li,[32] X. Li,[38] Y. Li,[43] Z. M. Li,[50] M. A. Lisa,[27] F. Liu,[50]
H. Liu,[4] J. Liu,[35] T. Ljubicic,[2] W. J. Llope,[35] R. S. Longacre,[2] W. A. Love,[2] Y. Lu,[37] E. V. Lukashov,[25] X. Luo,[37] G. L. Ma,[39]
Y. G. Ma,[39] D. P. Mahapatra,[12] R. Majka,[51] O. I. Mall,[4] L. K. Mangotra,[16] R. Manweiler,[45] S. Margetis,[18] C. Markert,[42]
H. Masui,[21] H. S. Matis,[21] Yu. A. Matulenko,[31] D. McDonald,[35] T. S. McShane,[8] A. Meschanin,[31] R. Milner,[22] N. G. Minaev,[31]
S. Mioduszewski,[41] A. Mischke,[26] M. K. Mitrovski,[11] B. Mohanty,[46] M. M. Mondal,[46] B. Morozov,[15] D. A. Morozov,[31]
M. G. Munhoz,[36] M. Naglis,[21] B. K. Nandi,[13] T. K. Nayak,[46] P. K. Netrakanti,[32] M. J. Ng,[3] L. V. Nogach,[31] S. B. Nurushev,[31]
G. Odyniec,[21] A. Ogawa,[2] K. Oh,[33] A. Ohlson,[51] V. Okorokov,[25] E. W. Oldag,[42] D. Olson,[21] M. Pachr,[9] B. S. Page,[14]
S. K. Pal,[46] Y. Pandit,[18] Y. Panebratsev,[17] T. Pawlak,[47] H. Pei,[7] T. Peitzmann,[26] C. Perkins,[3] W. Peryt,[47] S. C. Phatak,[12] P. Pile,[2]
M. Planinic,[52] M. A. Ploskon,[21] J. Pluta,[47] D. Plyku,[28] N. Poljak,[52] A. M. Poskanzer,[21] B. V. K. S. Potukuchi,[16] C. B. Powell,[21]
D. Prindle,[48] C. Pruneau,[49] N. K. Pruthi,[29] P. R. Pujahari,[13] J. Putschke,[51] H. Qiu,[20] R. Raniwala,[34] S. Raniwala,[34] R. L. Ray,[42]
R. Redwine,[22] R. Reed,[4] H. G. Ritter,[21] J. B. Roberts,[35] O. V. Rogachevskiy,[17] J. L. Romero,[4] A. Rose,[21] L. Ruan,[2] J. Rusnak,[10]
S. Sakai,[21] I. Sakrejda,[21] T. Sakuma,[22] S. Salur,[4] J. Sandweiss,[51] E. Sangaline,[4] J. Schambach,[42] R. P. Scharenberg,[32]
A. M. Schmah,[21] N. Schmitz,[23] T. R. Schuster,[11] J. Seele,[22] J. Seger,[8] I. Selyuzhenkov,[14] P. Seyboth,[23] E. Shahaliev,[17]
M. Shao,[37] M. Sharma,[49] S. S. Shi,[50] E. P. Sichtermann,[21] F. Simon,[23] R. N. Singaraju,[46] M. J. Skoby,[32] N. Smirnov,[51]
P. Sorensen,[2] J. Speltz,[40] H. M. Spinka,[1] B. Srivastava,[32] T. D. S. Stanislaus,[45] D. Staszak,[5] S. G. Steadman,[22] J. R. Stevens,[14]
R. Stock,[11] M. Strikhanov,[25] B. Stringfellow,[32] A. A. P. Suaide,[36] M. C. Suarez,[7] N. L. Subba,[18] M. Sumbera,[10] X. M. Sun,[21]
Y. Sun,[37] Z. Sun,[20] B. Surrow,[22] D. N. Svirida,[15] T. J. M. Symons,[21] A. Szanto de Toledo,[36] J. Takahashi,[6] A. H. Tang,[2]
Z. Tang,[37] L. H. Tarini,[49] T. Tarnowsky,[24] D. Thein,[42] J. H. Thomas,[21] J. Tian,[39] A. R. Timmins,[49] D. Tlusty,[10] M. Tokarev,[17]
T. A. Trainor,[48] V. N. Tram,[21] S. Trentalange,[5] R. E. Tribble,[41] P. Tribedy,[46] O. D. Tsai,[5] T. Ullrich,[2] D. G. Underwood,[1]
G. Van Buren,[2] G. van Nieuwenhuizen,[22] J. A. Vanfossen Jr.,[18] R. Varma,[13] G. M. S. Vasconcelos,[6] A. N. Vasiliev,[31]
F. Videbæk,[2] Y. P. Viyogi,[46] S. Vokal,[17] S. A. Voloshin,[49] M. Wada,[42] M. Walker,[22] F. Wang,[32] G. Wang,[5] H. Wang,[24]
J. S. Wang,[20] Q. Wang,[32] X. L. Wang,[37] Y. Wang,[43] G. Webb,[19] J. C. Webb,[2] G. D. Westfall,[24] C. Whitten Jr.,[5] H. Wieman,[21]
S. W. Wissink,[14] R. Witt,[44] W. Witzke,[19] Y. F. Wu,[50] W. Xie,[32] H. Xu,[20] N. Xu,[21] Q. H. Xu,[38] W. Xu,[5] Y. Xu,[37] Z. Xu,[2]
L. Xue,[39] Y. Yang,[20] P. Yepes,[35] K. Yip,[2] I-K. Yoo,[33] Q. Yue,[43] M. Zawisza,[47] H. Zbroszczyk,[47] W. Zhan,[20] J. B. Zhang,[50]
S. Zhang,[39] W. M. Zhang,[18] X. P. Zhang,[43] Y. Zhang,[21] Z. P. Zhang,[37] J. Zhao,[39] C. Zhong,[39] W. Zhou,[38] X. Zhu,[43] Y. H. Zhu,[39]
R. Zoulkarneev,[17] and Y. Zoulkarneeva[17]

(STAR Collaboration)

[1]*Argonne National Laboratory, Argonne, Illinois 60439, USA*
[2]*Brookhaven National Laboratory, Upton, New York 11973, USA*
[3]*University of California, Berkeley, California 94720, USA*
[4]*University of California, Davis, California 95616, USA*
[5]*University of California, Los Angeles, California 90095, USA*
[6]*Universidade Estadual de Campinas, Sao Paulo, Brazil*
[7]*University of Illinois at Chicago, Chicago, Illinois 60607, USA*
[8]*Creighton University, Omaha, Nebraska 68178, USA*
[9]*Czech Technical University in Prague, FNSPE, Prague, 115 19, Czech Republic*
[10]*Nuclear Physics Institute AS CR, 250 68 Řež/Prague, Czech Republic*
[11]*University of Frankfurt, Frankfurt, Germany*

^{12}*Institute of Physics, Bhubaneswar 751005, India*
^{13}*Indian Institute of Technology, Mumbai, India*
^{14}*Indiana University, Bloomington, Indiana 47408, USA*
^{15}*Alikhanov Institute for Theoretical and Experimental Physics, Moscow, Russia*
^{16}*University of Jammu, Jammu 180001, India*
^{17}*Joint Institute for Nuclear Research, Dubna, 141 980, Russia*
^{18}*Kent State University, Kent, Ohio 44242, USA*
^{19}*University of Kentucky, Lexington, Kentucky 40506-0055, USA*
^{20}*Institute of Modern Physics, Lanzhou, China*
^{21}*Lawrence Berkeley National Laboratory, Berkeley, California 94720, USA*
^{22}*Massachusetts Institute of Technology, Cambridge, Massachusetts 02139-4307, USA*
^{23}*Max-Planck-Institut für Physik, Munich, Germany*
^{24}*Michigan State University, East Lansing, Michigan 48824, USA*
^{25}*Moscow Engineering Physics Institute, Moscow Russia*
^{26}*NIKHEF and Utrecht University, Amsterdam, The Netherlands*
^{27}*Ohio State University, Columbus, Ohio 43210, USA*
^{28}*Old Dominion University, Norfolk, Virginia, 23529, USA*
^{29}*Panjab University, Chandigarh 160014, India*
^{30}*Pennsylvania State University, University Park, Pennsylvania 16802, USA*
^{31}*Institute of High Energy Physics, Protvino, Russia*
^{32}*Purdue University, West Lafayette, Indiana 47907, USA*
^{33}*Pusan National University, Pusan, Republic of Korea*
^{34}*University of Rajasthan, Jaipur 302004, India*
^{35}*Rice University, Houston, Texas 77251, USA*
^{36}*Universidade de Sao Paulo, Sao Paulo, Brazil*
^{37}*University of Science & Technology of China, Hefei 230026, China*
^{38}*Shandong University, Jinan, Shandong 250100, China*
^{39}*Shanghai Institute of Applied Physics, Shanghai 201800, China*
^{40}*SUBATECH, Nantes, France*
^{41}*Texas A&M University, College Station, Texas 77843, USA*
^{42}*University of Texas, Austin, Texas 78712, USA*
^{43}*Tsinghua University, Beijing 100084, China*
^{44}*United States Naval Academy, Annapolis, Maryland 21402, USA*
^{45}*Valparaiso University, Valparaiso, Indiana 46383, USA*
^{46}*Variable Energy Cyclotron Centre, Kolkata 700064, India*
^{47}*Warsaw University of Technology, Warsaw, Poland*
^{48}*University of Washington, Seattle, Washington 98195, USA*
^{49}*Wayne State University, Detroit, Michigan 48201, USA*
^{50}*Institute of Particle Physics, CCNU (HZNU), Wuhan 430079, China*
^{51}*Yale University, New Haven, Connecticut 06520, USA*
^{52}*University of Zagreb, Zagreb, HR-10002, Croatia*
(Received 1 October 2010; published 4 February 2011)

We present results on strange and multistrange particle production in Au + Au collisions at $\sqrt{s_{NN}} = 62.4$ GeV as measured with the STAR detector at RHIC. Midrapidity transverse momentum spectra and integrated yields of K_S^0, Λ, Ξ, and Ω and their antiparticles are presented for different centrality classes. The particle yields and ratios follow a smooth energy dependence. Chemical freeze-out parameters, temperature, baryon chemical potential, and strangeness saturation factor obtained from the particle yields are presented. Intermediate transverse momentum (p_T) phenomena are discussed based on the ratio of the measured baryon-to-meson spectra and nuclear modification factor. The centrality dependence of various measurements presented show a similar behavior as seen in Au + Au collisions at $\sqrt{s_{NN}} = 200$ GeV.

I. INTRODUCTION

Strange hadrons in the final products of high-energy nuclear collisions provide valuable insight into the properties of the created system, since they are not present inside the nuclei of the incoming beams. The production rates and phase-space distributions of the strange particles may reveal different characteristics of the created fireball and thus they have been studied at different accelerators and experiments [1–4].

The enhancement of strangeness production in relativistic heavy-ion collisions was first proposed as a signature of the quark gluon plasma (QGP) in the early 1980s [5]. The observation of an enhancement of strange baryon production relative to $p + p$ collisions in the CERN Super Proton Synchrotron (SPS) data [6–8], confirmed later by data from the Relativistic Heavy Ion Collider (RHIC) [9], has brought a lot of excitement to these studies.

While the production yields are mainly determined by the yields in the low transverse momentum region ($p_T < 2$ GeV/c), the intermediate transverse momentum region (p_T between 2 and 5 GeV/c) might give insight into the hadron production mechanism which in turn reveals important characteristics of the system. One of the most interesting results observed in this region is the apparent enhancement of baryons over mesons which was originally observed in the p/π ratio [10] but was also confirmed in the strangeness sector with the Λ/K_S^0 ratio [11]. Different theoretical scenarios to explain such behavior are discussed showing that detailed experimental data are needed to discriminate between these proposals.

We present in this article results on the production of K_S^0, Λ, Ξ, and Ω obtained by the STAR experiment at RHIC in Au + Au collisions at an energy of $\sqrt{s_{NN}} = 62.4$ GeV. This energy lies in the range between SPS and the highest RHIC energy and provides intermediate measurement points in the energy excitation functions. The systematic study with detailed measurement of the excitation function of various observables is very important for understanding the QCD phase diagram of nuclear matter and for the search for a critical point of the phase transition that would correspond to the end point of the first-order phase boundary as predicted by QCD [12,13].

The article is organized as follows. Section II is devoted to the STAR experimental apparatus used for the measurements and the event selection. The analysis techniques to reconstruct the decays of the strange particles are described in Sec. III along with the corrections needed to extract the physical spectra, the functional forms used to fit and integrate the p_T spectra, and the procedure used to calculate the systematic uncertainties. In Sec. IV the main results are presented and the physical implications of these measurements are discussed, including detailed comparisons to the corresponding data from Au + Au at 200-GeV collisions [9,14,15]. Chemical freeze-out properties are extracted from the particle ratios, strangeness enhancement is tested using the ratio of strange particles and pions, and baryon-to-meson differences are studied by comparing the K_S^0 spectra to the Λ spectra. Final remarks and an overview of the general behavior of strange particle production considering the collision energy dependence are presented in Sec. V.

II. EXPERIMENTAL APPARATUS

The data presented in this article were measured during the 2004 run of RHIC situated at Brookhaven National Laboratory (BNL) using the STAR detector. The data correspond to Au + Au collisions at $\sqrt{s_{NN}} = 62.4$ GeV. Descriptions and

references concerning the STAR detector and its subdetectors may be found in Ref. [16]. The main subsystem of the STAR detector used for this analysis is a cylindrical time projection chamber (TPC) (length 4.2 m, inner radius 0.5 m, outer radius 2 m) covering a pseudorapidity range of $|\eta| < 1.8$ with a 2π coverage in azimuth. The TPC is immersed in a magnetic field of 0.5 T parallel to the beam direction that enables the measurement of trajectories and momenta of charged particles with a transverse momentum (p_T) above 0.15 GeV/c. The TPC is filled with P10 gas (10% methane, 90% argon) regulated at 2 mbar above atmospheric pressure.

In addition to its track detection and momentum determination capabilities, the TPC provides particle identification for charged particles by measuring their ionization energy-loss (dE/dx) in the TPC gas. Details and performance of the energy-loss particle-identification method are explained in Ref. [17].

The collisions were triggered using a combination of several trigger detectors [18]. The minimum bias trigger requires coincidences between two zero-degree calorimeters (ZDC) located 18 m along the beam axis on each side of the interaction region. Beam-fragment (spectator) neutrons are not deflected by the beam guiding magnets and are thus detected in the ZDC detectors. In addition, a scintillation counter central trigger barrel (CTB) that surrounds the outer cylinder of the TPC was used to trigger on charged-particle multiplicity in the mid-pseudo-rapidity region. Two beam-beam counters were also used in the trigger system to measure the charged-particle multiplicity in the forward region ($3.3 < |\eta| < 5.0$).

The acquired data consist of a total of 6×10^6 minimum bias triggered events. In order to study the centrality dependence of strangeness production, these events were divided into centrality classes according to fractions of the total inelastic collision cross section. The centrality of an event was defined as in previous analyses [14] by the measured (uncorrected) multiplicity in the TPC of charged tracks with specific quality cuts.

In this analysis, only events with a primary vertex position within ± 30 cm from the center of the TPC along the beam line were used to ensure a good rapidity coverage and relative uniformity of the detector efficiency. All the results quoted in this article are midrapidity ($|y| < 1.0$) results.

For each event centrality class, the equivalent collision impact parameter is estimated based on a comparison between the measured uncorrected charged-particle multiplicity $dN_{ch}/d\eta$ and the calculated cross section using a Monte Carlo Glauber approach [19]. In this approach, it is possible to determine for each centrality class the average number of participant nucleons $\langle N_{part} \rangle$ (number of nucleons that have at least one interaction in the collision) and the average number of nucleon-nucleon binary collisions $\langle N_{bin} \rangle$ that occur during a Au + Au collision. These quantities are calculated considering the trajectory of nucleons in a nuclei as straight lines and that a interaction occurs when the distance between two nucleons is less than the one given by the total inelastic nucleon-nucleon cross section in the plane orthogonal to the beam axis. Table I shows the $\langle N_{part} \rangle$ and $\langle N_{bin} \rangle$ together with the midrapidity charged-particle yields dN_{ch}/dy for all centrality classes.

TABLE I. Summary of the centrality classes used to separate the events in this analysis. For each centrality class, the equivalent mean number of participant nucleons $\langle N_{\text{part}} \rangle$ and the mean number of binary collisions are determined using the charged-particle multiplicity distributions and a Monte Carlo Glauber model. Also shown in this table is the corrected charged-particle multiplicity density $\langle dN_{\text{ch}}/dy \rangle$ that was obtained by adding the yields of protons, antiprotons, charged pions, and charged kaons. Details of the analysis can be found in Ref. [14].

	0–5%	5–10%	10–20%	20–30%	30–40%	40–60%	60–80%
$\langle N_{\text{part}} \rangle$	346.5 ± 2.8	293.9 ± 4.2	229.8 ± 4.6	164.1 ± 5.4	114.3 ± 5.1	62.0 ± 4.9	21.4 ± 3.0
$\langle N_{\text{bin}} \rangle$	891 ± 57	710 ± 47	511 ± 34	325 ± 23	199 ± 16	88 ± 10	22 ± 4
$\langle dN_{\text{ch}}/dy \rangle$	582 ± 38	476 ± 30	359 ± 24	249 ± 16	166 ± 11	86 ± 7	27 ± 2

III. ANALYSIS

The analysis methods for the different particle species are detailed in the following sub-sections. The K_S^0 and Λ reconstruction method is described in Sec. III A. The reconstruction of multistrange particles through the correlation of three particles is described in Sec. III B.

A. K_S^0 and Λ reconstruction

K_S^0, Λ, and $\bar{\Lambda}$ were identified through the reconstruction of the weak decay topology:

$$K_S^0 \rightarrow \pi^+ + \pi^-$$

(branching ratio 69.20%) and

$$\Lambda \rightarrow p + \pi^-$$
$$\overline{\Lambda} \rightarrow \bar{p} + \pi^+$$

(branching ratio 63.9%).

The weak decay daughter candidates were selected using dE/dx information to reduce the combinatoric background of the invariant mass spectra. The dE/dx information can discriminate protons from pions and kaons up to a momentum of approximately 800 MeV. Hence, the dE/dx selection helps to reduce the background mainly in the lower-p_T region. In this analysis, a residual cut of three σs to the mean value of the energy loss equivalent to the identified particle was used and the overall background of the invariant mass spectra under the K_S^0 peak was reduced by a factor of 12% and by 70% for the Λs. In addition to the dE/dx information, geometrical cuts such as the distance of closest approach (DCA) between the two daughter tracks and the pointing vector of the daughter tracks (distance of closest approach of the projected helix trajectory) away from the primary vertex position were used to improve the signal-to-noise ratio of the invariant mass peaks. A geometrical cut on the extrapolation of the reconstructed Λ trajectory from the primary vertex position was also used to reduce the contribution of feed-down Λ particles such as those from the Ξ sequential decay. Cut selection was optimized considering a compromise between background minimization and signal efficiency in the high-p_T bins. Table II shows the geometrical cuts used in this analysis.

The invariant mass distributions of the reconstructed particles, obtained after the geometrical and particle identification cuts, are presented in Fig. 1(a) for K_S^0 and panel (b) for Λ and $\overline{\Lambda}$. The remaining background underneath the mass peak was subtracted by making an interpolation of the spectrum on either side of the mass peak. Various polynomial functions were fitted to the background to estimate a systematic uncertainty for the signal area. The difference in the background estimated using the two different methods was used in the calculation of the systematic uncertainty for each point in the final p_T spectra. In general, the shape of the background in the invariant mass spectra was smooth and relatively flat which resulted in uncertainties below 3%. The signal itself was then determined by counting the entries in the bins contributing to the peak and subtracting the estimated background.

B. Ξ and Ω reconstruction

The multistrange hyperons were reconstructed via the topology of their weak decays:

$$\Xi^- \rightarrow \Lambda + \pi^-$$
$$\bar{\Xi}^+ \rightarrow \overline{\Lambda} + \pi^+$$

(branching ratio 99.887%) and

$$\Omega^- \rightarrow \Lambda + K^-$$
$$\bar{\Omega}^+ \rightarrow \overline{\Lambda} + K^+$$

(branching ratio 67.8%).

Λ candidates reconstructed as described in the previous section are combined with single track, assuming it to be the bachelor $\pi^\pm$ for the Ξ decays and $K^\pm$ for the Ω decays. Here, the dE/dx information was crucial to reduce the combinatoric background. The Ω peak in the invariant mass spectra was identifiable only when using the dE/dx selection on the kaon bachelor candidates.

Despite the identification of the daughters by their dE/dx, geometric selections were also used to improve the purity of the samples due to the large combinatorial background. These selections were done by cutting sequentially on the different variables aiming for a compromise between background minimization and signal efficiency in the high-p_T bins. Table III shows the geometrical cuts used in this analysis. The

TABLE II. Geometrical cuts used in the analysis of K_S^0 and $\Lambda(\bar{\Lambda})$ production.

Cut	K_s^0	Λ and $\bar{\Lambda}$
DCA of V0 to primary vertex	<0.5 cm	< 0.8 cm
DCA of V0 daughters to primary vertex	>0.8 cm	>1.0 cm
DCA between V0 daughters	<0.8 cm	<0.8 cm
Number of hits in the daughters trajectory	$\geqslant 15$	$\geqslant 15$
Radial decay length	>4 cm	>5 cm
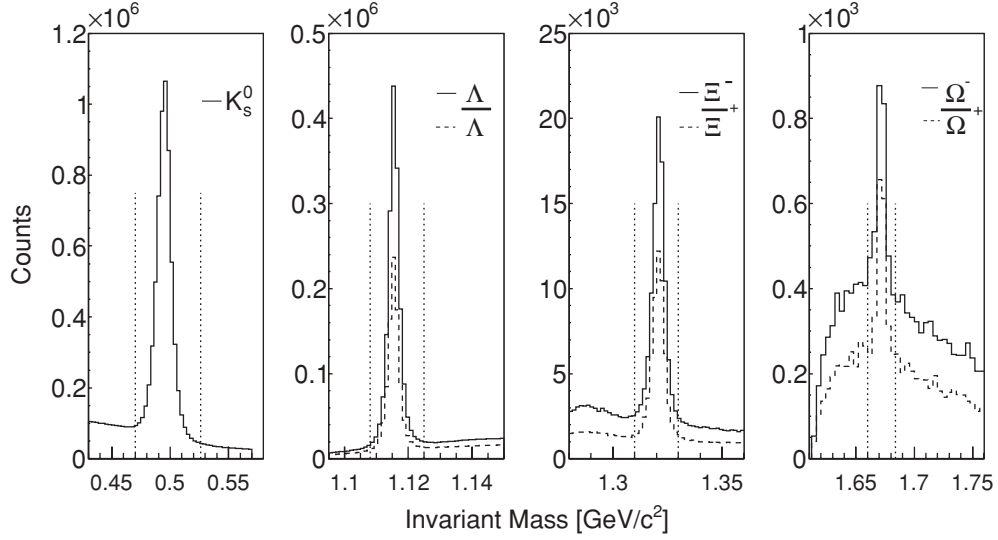
FIG. 1. Invariant mass distributions for selected candidates for (a) K_S^0, (b) Λ, $\overline{\Lambda}$, (c) Ξ^-, $\bar{\Xi}^+$, and (d) Ω^-, $\bar{\Omega}^+$ (note the different scaling factors for Λ, Ξ, and Ω) for rapidity interval $|y| < 1.0$ and $p_T > 0.2$ GeV/c. The limits represented by the vertical dotted lines are the ones used for signal counting.

invariant mass of the assumed parent particle obtained from the candidates passing the selection cuts was calculated and plotted in a histogram, as shown in Fig. 1(c) for the Ξ and Fig. 1(d) for the Ω.

Even after the cut optimization, some background still remained in the invariant mass distributions. The background under the invariant mass peak was estimated using the same method as used for the Λ analysis, where polynomial functions were used to parametrize the background outside the peak region. The background estimated by a polynomial fit function was subtracted from the invariant mass spectra in order to calculate the raw yield. In the following step, the raw spectra were corrected for the detector and analysis inefficiencies.

C. Correction factors

These corrections include tracking efficiency and detector acceptance as well as reconstruction inefficiencies. The correction factors were determined as a function of p_T and the efficiencies for the different particles were calculated in

different rapidity intervals between -1 and $+1$ to verify that these corrections were independent of rapidity. The corrections were estimated by using Monte Carlo–generated particles which were propagated through a TPC detector response simulator and embedded into real events on the cluster level. These enriched events were then reconstructed using the usual reconstruction chain. The correction factors for the different particles obtained by this method are shown as a function of p_T in Fig. 2.

The measured Λ spectra were also corrected for feed-down of weak decays by subtracting the contributions from the charged and neutral Ξ decays. As mentioned in Sec. III A, a geometrical cut on the distance of closest approach between the extrapolated reconstructed track of the Λ and the primary vertex position was used to reduce this contribution. Nevertheless, some of the secondary Λ still satisfied this cut, especially in the high-p_T region. The relative number of Λ particles from the Ξ decays that were in the primary particle sample was estimated using embedded Monte Carlo Ξ to calculate the reconstruction efficiency of these secondary Λ particles, which was then

TABLE III. Geometrical cuts used in the analysis of the production of Ξ, Ω and their antiparticles.

Cut	Ξ^- and $\bar{\Xi}^+$	Ω^- and $\bar{\Omega}^+$
DCA of parent to primary vertex	<0.6 cm	<0.6 cm
DCA of bachelor to primary vertex	>1.0 cm	$> 1.6 \times \sqrt{\text{DCA of parent to primary vertex}} + 0.1$ cm
DCA of V0 to primary vertex	>0.5 cm	$> 1.4 \times \sqrt{\text{DCA of parent to primary vertex}} + 0.1$ cm
DCA of positive V0 daughter to primary vertex	>0.7 cm	-
DCA of negative V0 daughter to primary vertex	>3.0 cm	-
DCA between V0 and bachelor	<0.8 cm	<0.6 cm
DCA between V0 daughters	<0.7 cm	<0.6 cm
Number of hits in the daughters trajectory	$\geqslant 15$	$\geqslant 25$
Parent decay length	>5 cm	>3 and < 20 cm
V0 decay length	—	>2 and < 30 cm and $> -4 * \sqrt{\Xi \text{ decay length}} + 23$ cm
Daughter V0 inv. mass	1.1175 ± 0.0125 GeV/c^2	1.1150 ± 0.0070 GeV/c^2
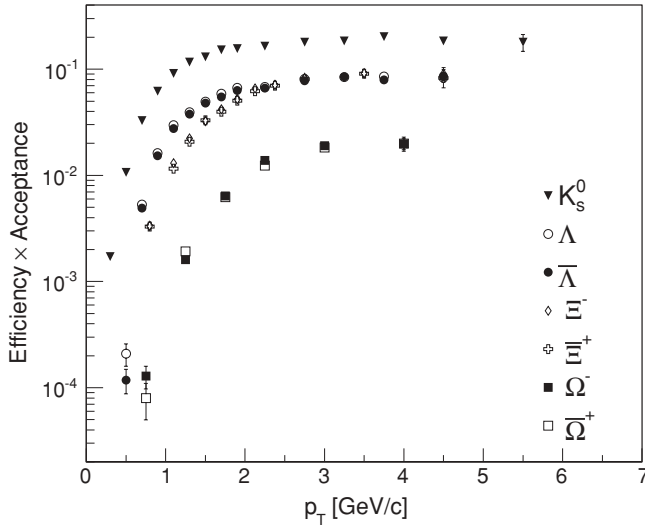
FIG. 2. Correction factors (acceptance × efficiency) for the most central events (0–5% for K_S^0, Λ, and Ξ; 0–20% for Ω) at midrapidity ($|y| < 1$) as a function of p_T for the different particle species as obtained via embedding. The branching ratio of the measured decay channel is not factored into this plot.

scaled by the corrected yield of the measured Ξ particles. The relative contribution of the feed-down was calculated for each p_T interval and in the high-p_T region was around 12%. Neutral Ξ was not measured by the STAR experiment. Thus, to calculate the feed-down from these particles, the yield of the neutral Ξ was considered to be equal to the yield of the $\Xi^{\pm}$ particles. The feed-down correction of the Λ spectra from the Ω decay was not considered since it is negligible due to the lower yield of the Ω particles. The contribution from the Σ_0 decay to the Λ yield was not subtracted as well due to the lack of Σ^0 yields measurements.

D. Extrapolation of the p_T spectra

The final spectra for each particle species were obtained by dividing the raw-yield p_T distribution by the correction factors presented in the last section.

As the spectra were not measured at low p_T due to the limited acceptance coverage and at high p_T due to the finite statistics, the spectra needed to be extrapolated in these two regions in order to determine the total production yield (dN/dy) as well as the mean transverse momentum ($\langle p_T \rangle$). This extrapolation was done with two different functional forms, an exponential function:

$$\frac{d^2N}{2\pi p_T dp_T dy} \propto e^{-\frac{m_T}{T}} \tag{1}$$

and a Maxwell-Boltzmann function:

$$\frac{d^2N}{2\pi p_T dp_T dy} \propto m_T e^{-\frac{m_T}{T}}. \tag{2}$$

The spectra were better described with a Maxwell-Boltzmann function, resulting in fits with lower χ^2 values than the exponential function fits. In addition, the

Maxwell-Boltzmann function was also used in the analysis of the data from Au + Au collisions at 200 GeV and thus allows for a consistent comparison between the two data sets.

The main contribution for the determination of the dN/dy comes from the low-p_T region of the spectra. Therefore, in order to have a better estimate of the spectra shape in the low-p_T region the fit was performed considering only the region of p_T smaller than 1.5 GeV/c. This extrapolation varied from 5 to 30% of the final total yield for most particle species. In the case of the Ω particles, the extrapolated yield was on the order of 50%, thus, the systematic uncertainty due to the extrapolation is large. The final dN/dy was obtained by integrating the data in the measured region and using the fitted function in the low-p_T region. The contribution of the high-p_T region to the dN/dy was verified and found to be negligible. The difference in the total integrated dN/dy using the Maxwell-Boltzmann and the exponential function was considered to be the systematic uncertainty due to the extrapolation.

The $\langle p_T \rangle$ is obtained by integrating the whole range of the p_T spectra as follows:

$$\langle p_T \rangle = \frac{\int p_T \frac{dN}{dp_T} dp_T}{\int \frac{dN}{dp_T} dp_T}. \tag{3}$$

The same functional forms used to determine the total yield were used to extrapolate the yield of the spectra in the unmeasured low-p_T region to calculate the $\langle p_T \rangle$. The final uncertainty of the $\langle p_T \rangle$ values was estimated considering the variation of the point-to-point uncertainties of the measured particle spectra, and the uncertainty in the contribution from the extrapolated low-p_T region.

E. Systematic uncertainties due to the correction factors

Several sources of systematic uncertainties were evaluated and identified in the analysis. Variations in the detector performance and trigger efficiency during data taking and the dependence on position of the primary vertex were checked and found to be negligible. The main sources of the systematic uncertainties were the uncertainties in the correction factors of the measured spectra.

In order to estimate the uncertainty due to the corrections of detector acceptance and efficiency of the analysis cuts, a careful comparison was performed between the distributions of the geometrical parameters obtained from the embedded simulated particles and the distributions of the tracks from real data. A good agreement between the data and the simulated embedded distributions was obtained. The systematic uncertainties were calculated assuming a finite resolution to determine the cut value applied to the embedded sample during the correction factor calculation. The values of the cut were varied randomly given a certain assumed resolution and new correction factors were calculated. Next, the particle yields were obtained from these new correction factors. The variation of the yields obtained from this procedure was considered as one of the sources of the systematic uncertainty. This uncertainty was less than 10% from all centrality bins.
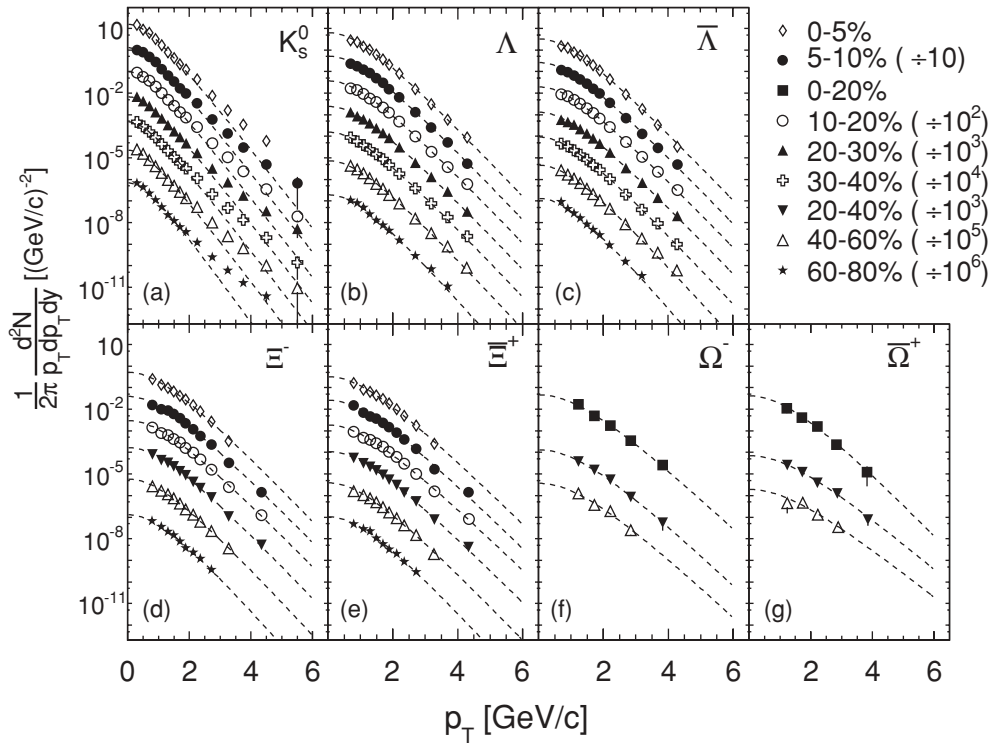
FIG. 3. Efficiency corrected p_T spectra for the different centrality bins and for the various particles. Note that seven centrality bins have been used for the K_S^0 and the Λ while only six and three have been used for the Ξ and Ω, respectively. Errors are statistical only. The Λ spectra are corrected for the feed-down of the Ξ decay.

IV. RESULTS AND DISCUSSIONS

The corrected p_T spectra for K_S^0, Λ, Ξ, and Ω and their antiparticles are presented in Fig. 3. For better visualization, the spectra were divided by factors of 10 from central to peripheral data. The normalization factors are indicated in the figure.

The shape of the spectra in the low-p_T region is sensitive to the characteristics of the evolution of the fireball such as transverse flow and the conditions of the kinetic freeze-out. With the increase in the momentum, the shape of the spectra is also affected by soft jets, whose fractional contribution to the shape of the spectra increases with increasing momentum. The variations in the shape of the p_T spectra for different particles and different centrality classes can be better visualized by examining the $\langle p_T \rangle$ values. The $\langle p_T \rangle$ calculated from the data, using a Maxwell-Boltzmann function to extrapolate for the

unmeasured low-p_T region, is presented in Table IV. The difference in the calculated $\langle p_T \rangle$ between using a Maxwell-Boltzmann or an exponential function is presented as the systematic uncertainty. Figure 4 shows the evolution of $\langle p_T \rangle$ as a function of dN_{ch}/dy (see Table I) for different particle species.

The $\langle p_T \rangle$ values for $\bar\Lambda$ and $\bar\Xi^+$ are equal within uncertainties to the $\langle p_T \rangle$ for Λ and Ξ^-, respectively, and thus they are not plotted in Fig. 4. The $\langle p_T \rangle$ values from the Ω spectra are not included in this comparison due to the large uncertainties. The $\langle p_T \rangle$ for $\pi^\pm$, $K^\pm$, and $\bar p$ shown in Fig. 4 were presented in Ref. [14]. Error bars of each point correspond to the statistical uncertainty while the systematic uncertainty from the extrapolation is represented by the gray bands.

The $\langle p_T \rangle$ values of K_S^0 are in agreement with the values of K^- and the Λ values with those of $\bar p$ spectra. The $\langle p_T \rangle$

TABLE IV. Average transverse momenta, $\langle p_T \rangle$, in GeV/c, for the strange hadrons from Au + Au collisions at 62.4 GeV. The first error is statistical, while the second is the systematic error arising from the extrapolation in the low-p_T region.

|	K_S^0	Λ	$\overline{\Lambda}$	Ξ^-	$\bar{\Xi}^+$
0–5%	$0.684 \pm 0.030 \pm 0.023$	$0.901 \pm 0.041 \pm 0.026$	$0.885 \pm 0.043 \pm 0.023$	$1.097 \pm 0.037 \pm 0.043$	$1.130 \pm 0.048 \pm 0.050$
5–10%	$0.694 \pm 0.027 \pm 0.023$	$0.899 \pm 0.039 \pm 0.026$	$0.892 \pm 0.036 \pm 0.025$	$1.136 \pm 0.040 \pm 0.056$	$1.136 \pm 0.048 \pm 0.050$
10–20%	$0.681 \pm 0.024 \pm 0.023$	$0.902 \pm 0.028 \pm 0.026$	$0.887 \pm 0.026 \pm 0.025$	$1.115 \pm 0.028 \pm 0.049$	$1.130 \pm 0.037 \pm 0.052$
20–30%	$0.660 \pm 0.034 \pm 0.023$	$0.886 \pm 0.032 \pm 0.024$	$0.892 \pm 0.025 \pm 0.026$	$1.068 \pm 0.025 \pm 0.042$	$1.042 \pm 0.031 \pm 0.035$
30–40%	$0.658 \pm 0.036 \pm 0.022$	$0.862 \pm 0.035 \pm 0.021$	$0.849 \pm 0.029 \pm 0.020$		
40–60%	$0.627 \pm 0.038 \pm 0.022$	$0.823 \pm 0.035 \pm 0.015$	$0.807 \pm 0.032 \pm 0.013$	$0.975 \pm 0.039 \pm 0.029$	$1.022 \pm 0.047 \pm 0.041$
60–80%	$0.611 \pm 0.062 \pm 0.022$	$0.772 \pm 0.058 \pm 0.010$	$0.766 \pm 0.075 \pm 0.010$	$0.869 \pm 0.074 \pm 0.013$	$0.90 \pm 0.11 \pm 0.02$
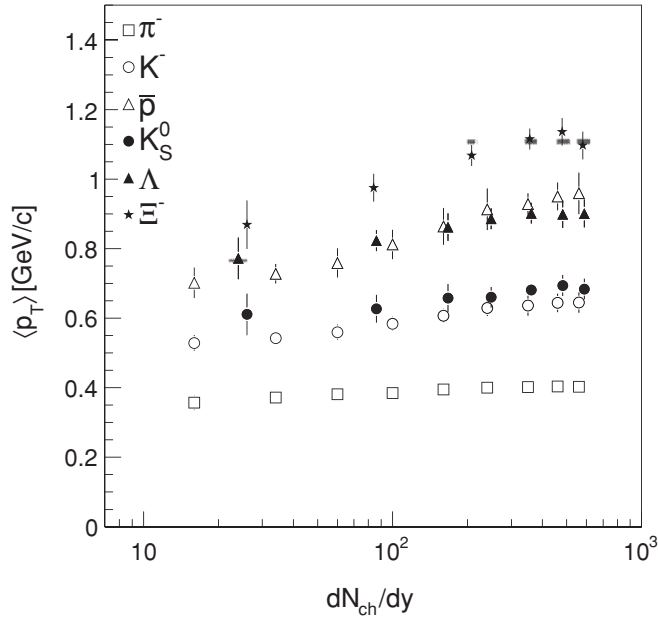
FIG. 4. Extrapolated average transverse momenta $\langle p_T \rangle$ as a function of dN_{ch}/dy for different particle species in Au + Au collisions at 62.4 GeV. Statistical uncertainties are represented by the error bars at the points while the systematic uncertainties are represented by the gray bars. The π, charged K and p data were extracted from Ref. [14].

shows a trend of increase from peripheral to central collisions for all particles. This increase is more pronounced for the heavier particles ($\bar{p}$) than for the lighter particles (π). These observations are consistent with a collective radial flow among formed hadrons, which increases with centrality.

The integrated yields for each centrality selection for the K_S^0, Λ, and $\bar{\Lambda}$ are presented in Table V while the yields for the Ξ^-, $\bar{\Xi}^+$, Ω^-, and $\bar{\Omega}^+$ are presented in Table VI. The systematic uncertainties correspond to the uncertainties due to the correction factors and the uncertainty due to the extrapolation.

STAR experiment has presented $K^{\pm}$ yields and spectra for the same colliding system in Ref. [14]. For the most central events, the integrated yields of K_S^0 is lower than the average between the integrated yields of K^+ and K^-. Figure 5 shows the comparison of the K_S^0 and $K^{\pm}$ $d^2N/dydp_T$

spectra in both top 5% and 30–50% centrality bins. The data points are consistent within uncertainties for the p_T range of 0.6–0.8 GeV/c but the K_S^0 data points are significantly lower for the two lowest p_T bins. The difference is no larger than two σ s. The charged kaon spectra is limited by the dE/dx identification method to a maximum p_T of 0.75 GeV/c. In addition, the charged kaon yields presented in Ref. [14] are measured in the rapidity interval of $|y| < 0.1$, whereas the K_S^0 yields presented are for rapidity interval of $|y| < 1.0$. We also note that the difference between the charged kaon spectra and the K_S^0 spectra decrease with decreasing centrality and in the peripheral bin of 30–40% the data points are in agreement within the experimental error bars for all p_T points in the overlap region.

Figure 6 shows the dependence of the singly strange and multistrange particle yields on the collision energy, including the results from this analysis. The lowest energy points are from Au + Au collisions measured by the E896 experiment at the BNL Alternating Gradient Synchrotron (AGS) [1] and the points in the SPS energy region are from Pb + Pb collisions measured by the NA49 experiment [20] and the NA57 experiment [2]. The RHIC data points for 130 and 200 GeV [15,21] are also presented. The strange baryon and meson production exhibits only a small energy dependence from AGS through SPS and on up to the top RHIC energies. From the AGS energy to the top SPS energy region, the Λ yield seems to increase at first, reaching a maximum around $\sqrt{s_{NN}} \approx 10$ GeV, and then starts to decrease slightly with energy. At RHIC the yield of Λ seems to stay approximately constant, independent of the collision energy.

Meanwhile, the Ω and the antibaryon yields show a clear and smooth rise with energy. The overall trend of the strange and multistrange antiparticle yields with energy indicates a transition from a transport-dominated production mechanism at the lower energies (AGS and SPS) to a production dominated by quark pair creation at the top RHIC energy. Transport dominated means that the initial baryon number of the colliding nuclei is transported to the midrapidity region. This transition occurs in a way that the midrapidity baryon-free regime is reached smoothly.

Figure 7 shows the antibaryon-to-baryon ratio of Λ, Ξ, and Ω baryons as a function of energy which can be seen to reach almost unity for all particle species at $\sqrt{s_{NN}} = 200$ GeV. The dashed lines in Fig. 7 show the results of a thermal model calculation [22] that will be discussed in Sec. IV A.

TABLE V. Integrated yield, dN/dy, for K_S^0, Λ, and $\bar{\Lambda}$ measured in Au + Au collisions at 62.4 GeV using data and a Maxwell-Boltzmann function for the extrapolation to the unmeasured low p_T region. Quoted uncertainties are the statistical errors and the systematic uncertainties. The Λ and $\bar{\Lambda}$ yields are corrected by subtracting the contribution of the feed-down from the Ξ weak decays.

	K_S^0	Λ	$\bar{\Lambda}$
0–5%	$27.4 \pm 0.6 \pm 2.9$	$15.7 \pm 0.3 \pm 2.3$	$8.3 \pm 0.2 \pm 1.1$
5–10%	$21.9 \pm 0.5 \pm 2.3$	$12.2 \pm 0.3 \pm 1.9$	$6.1 \pm 0.1 \pm 0.8$
10–20%	$17.1 \pm 0.3 \pm 1.7$	$9.1 \pm 0.2 \pm 1.3$	$4.7 \pm 0.1 \pm 0.6$
20–30%	$12.1 \pm 0.3 \pm 1.1$	$6.2 \pm 0.1 \pm 0.8$	$2.99 \pm 0.05 \pm 0.40$
30–40%	$8.1 \pm 0.2 \pm 0.7$	$4.1 \pm 0.1 \pm 0.6$	$2.25 \pm 0.04 \pm 0.30$
40–60%	$4.0 \pm 0.1 \pm 0.3$	$2.01 \pm 0.04 \pm 0.26$	$1.16 \pm 0.02 \pm 0.16$
60–80%	$1.13 \pm 0.05 \pm 0.09$	$0.504 \pm 0.017 \pm 0.07$	$0.343 \pm 0.012 \pm 0.036$

TABLE VI. Integrated midrapidity yield, dN/dy, for Ξ^-, $\bar{\Xi}^+$, Ω^-, and $\bar{\Omega}^+$ measured in Au + Au collisions at 62.4 GeV (using a Maxwell-Boltzmann function for the extrapolation). Quoted uncertainties are the statistical errors and the systematic uncertainties.

	Ξ^-	$\bar{\Xi}^+$	Ω^-	$\bar{\Omega}^+$
0–5%	$1.63 \pm 0.09 \pm 0.18$	$1.03 \pm 0.09 \pm 0.11$		
5–10%	$1.16 \pm 0.06 \pm 0.16$	$0.86 \pm 0.08 \pm 0.12$	$0.212 \pm 0.028 \pm 0.018$	$0.167 \pm 0.027 \pm 0.015$
10–20%	$0.96 \pm 0.04 \pm 0.11$	$0.59 \pm 0.03 \pm 0.06$		
20–40%	$0.52 \pm 0.02 \pm 0.06$	$0.357 \pm 0.016 \pm 0.037$	$0.056 \pm 0.006 \pm 0.005$	$0.038 \pm 0.005 \pm 0.003$
40–60%	$0.183 \pm 0.008 \pm 0.021$	$0.116 \pm 0.005 \pm 0.017$	$0.0165 \pm 0.0027 \pm 0.0014$	$0.0103 \pm 0.0020 \pm 0.0010$
60–80%	$0.042 \pm 0.003 \pm 0.005$	$0.032 \pm 0.003 \pm 0.004$		

Figure 8 shows the antibaryon-to-baryon ratio of p, Λ, and Ξ baryons as a function of the centrality of the collisions, represented by the measured number of charged hadrons per unit of rapidity (dN_{ch}/dy). Results from $\sqrt{s_{NN}} = 200$ GeV collisions (open symbols) and from the $\sqrt{s_{NN}} = 62.4$ GeV collisions (solid symbols) are compared. At $\sqrt{s_{NN}} = 62.4$ GeV, the $\bar{p}/p$ and $\bar{\Lambda}/\Lambda$ ratios show a similar trend, decreasing with increasing centrality, consistent with a higher degree of baryon number transport from beam rapidity for central collisions. The decrease with centrality seems to be larger at 62.4 GeV than at 200 GeV, which is consistent with a higher fraction of net-baryons being transported from beam rapidity to midrapidity at the lower collision energies. At $\sqrt{s_{NN}} = 200$ GeV where there is a wider rapidity gap between the beam particles, the net-baryon density at midrapidity is lower, thus, the antibaryon-to-baryon ratios of the studied particles are higher than at 62.4 GeV. In addition, the ratio is independent of centrality at $\sqrt{s_{NN}} = 200$ GeV, indicating that pair production is dominating and that there is a smaller variation of net-baryon density with centrality.

A. Chemical properties

The chemical properties of the bulk particle production can be addressed by using thermal-statistical models [23–27]. They are applicable under the assumption that the yields of particles are governed by statistical laws. The particle abundance of species i per system volume (N_i/V) can be parameterized by:

$$\frac{N_i}{V} = \frac{g_i}{(2\pi)^3} \int \left[\gamma_S^{-|S_i'|} \exp\left(\frac{E_i - \mu_i}{T_{ch}}\right) \pm 1 \right]^{-1} d^3p, \quad (4)$$
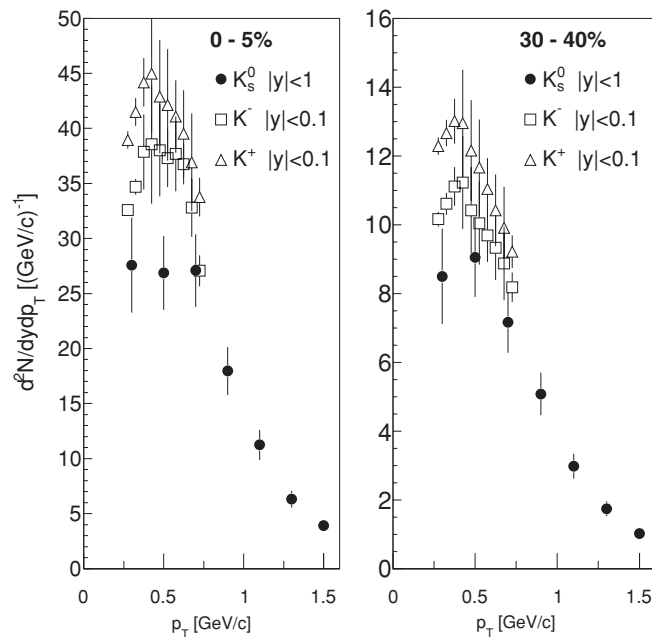

FIG. 5. K_S^0 dN/dp_T spectra compared to the charged kaon spectra for the event centrality of 0–5% and 30–40%. The charged kaons data points are for rapidity range of $|y| < 0.1$ and were extracted from Ref. [14].
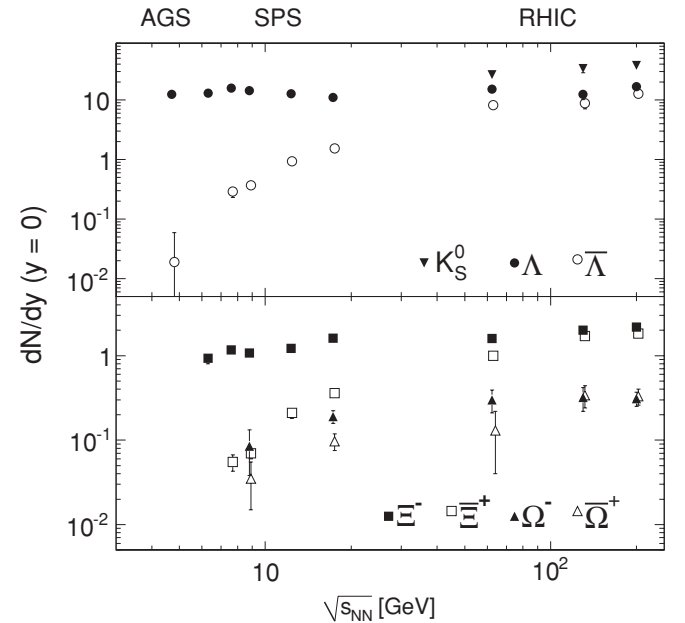

FIG. 6. Strange particle production yields at midrapidity in central Au + Au and Pb + Pb collisions versus the center-of-mass energy $\sqrt{s_{NN}}$. The top panel shows results for K_S^0 and Λ. The BNL Alternating Gradient Synchrotron (AGS) values are from E896 [1] (centrality 0–5%). The SPS values are from NA49 [20] (centrality 0–7%) and the RHIC values are from STAR [4,15] (centrality 0–5%). For the multistrange baryons Ξ and Ω (bottom), the SPS results are from NA57 [2] (centrality 0–11%) and the RHIC values are from STAR [15,21] (centrality 0–20%).
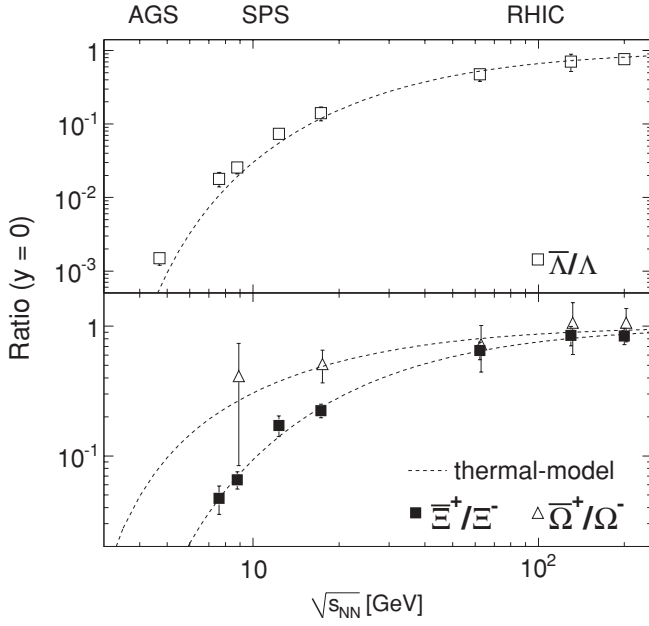
FIG. 7. Antibaryon to baryon yield ratios for strange baryons versus the center of mass energy $\sqrt{s_{NN}}$. $\overline{\Lambda}/\Lambda$ is shown in the top panel while the multistrange baryons are on the bottom panel. The data from AGS are not corrected for the weak decay feed-down from the multistrange baryons while the data from SPS and RHIC are corrected. The lines are the results of a thermal model calculation (see Sec. IV A). The AGS values are from E896 [1] (centrality 0–5%). The SPS values are from NA49 [20] (centrality 0–7%) and the RHIC values are from STAR [4,15] (centrality 0–5%). For the multistrange baryons Ξ and Ω (bottom), the SPS results are from NA57 [2] (centrality 0–11%) and the RHIC values are from STAR [15,21] (centrality 0–20%).

where

$$\mu_i = \mu_B B_i - \mu_Q Q_i - \mu_S S_i \tag{5}$$

and the g_i factor is the spin-isospin degeneracy; T_{ch} is the chemical freeze-out temperature that marks the end of inelastic interactions; μ_Q, μ_B, and μ_S are the charge, baryon, and strangeness chemical potentials, respectively; B_i, Q_i, and S_i are the baryon, charge, and strangeness numbers; E_i is the energy of the particle; γ_s is the strange quark phase-space occupancy; and S'_i is the number of valence strange and antistrange quarks in the particle i.

These thermal-statistical models have been successful in reproducing the particle ratios for a large range of energies and also have been able to reproduce ratios, including strange and multistrange particles such as the Ω/π ratio [28,29]. The evolution of the antibaryon-to-baryon ratio of the studied particles with $\sqrt{s_{NN}}$ is also well reproduced in these models as indicated in Fig. 7 by the dashed lines. These lines correspond to the antibaryon-to-baryon ratios using a thermal model calculation with parameters (temperature and chemical potentials) given by the systematic study presented in Ref. [30]. The data at the intermediate 62.4-GeV energy are also well reproduced.

In order to perform a thermal fit to the STAR data, we used the model THERMUS described in Ref. [31]. The parameters
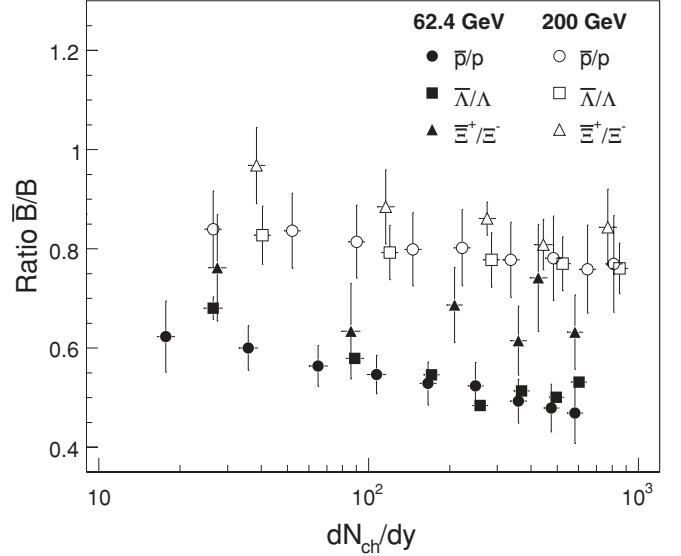

FIG. 8. Antibaryon-to-baryon yield ratios for strange particles and protons as a function of dN_{ch}/dy at $\sqrt{s_{NN}} = 62.4$ and 200 GeV. The p data were extracted from Ref. [14]. The $\sqrt{s_{NN}} = 200$ GeV strange hadron data were extracted from Ref. [15].

considered in this thermal fit are the temperature (T_{ch}), the baryon chemical potential (μ_B), and the strangeness saturation factor (γ_s). The strangeness chemical potential (μ_s) was constrained by the initial S/V ratio (strangeness per volume). The charge chemical potential (μ_Q) was fixed to zero and the system volume was not considered because particle ratios were used. To calculate the particle ratios, proton yields were corrected to subtract the contributions from the weak decays of Λ particles. The feed-down contribution from the Σ decay into the proton and antiproton yields were done within the thermal model and the correction was on the order of 7%. The pions were corrected for the weak decay feed-down, muon contamination and background pions produced in the detector materials. The Λ yields were corrected for the weak decay feed-down from the Ξ. Figure 9 shows the particle ratios as obtained by measurements for the most central data as black dots.

The fit procedure was performed with two different data sets, considering first only the particle ratios of p, $\bar{p}$, $\pi^\pm$, and $K^\pm$. Results from this fit are shown in Fig. 9 as dashed lines (blue online) and it is seen that the model fits quite well the ratios of pions, protons, and charged kaons, but it underpredicts the ratio $\bar{\Xi}^+/\Xi^-$. The thermal fit was repeated considering also the particle ratios with Λ, $\bar{\Lambda}$, and $\Xi^\pm$. The Ω ratios were not included in these thermal fits because the yields were obtained for different event centrality bins due to limited statistics in data. The results of the thermal fit, including the Λ and Ξ ratio, are also shown in Fig. 9 by the full lines (green online). The standard deviations of the data to the thermal fit result are also shown at the bottom of Fig. 9. Most of the results are within 1 standard deviation from the data for the case where the strange particle ratios are also considered in the calculation. The inclusion of the strange baryons in the thermal studies results in a more constrained fit and a better description of these yields. In addition, there is a small increase of T_{ch} from (147 ± 7) MeV to (163 ± 5) MeV but the value
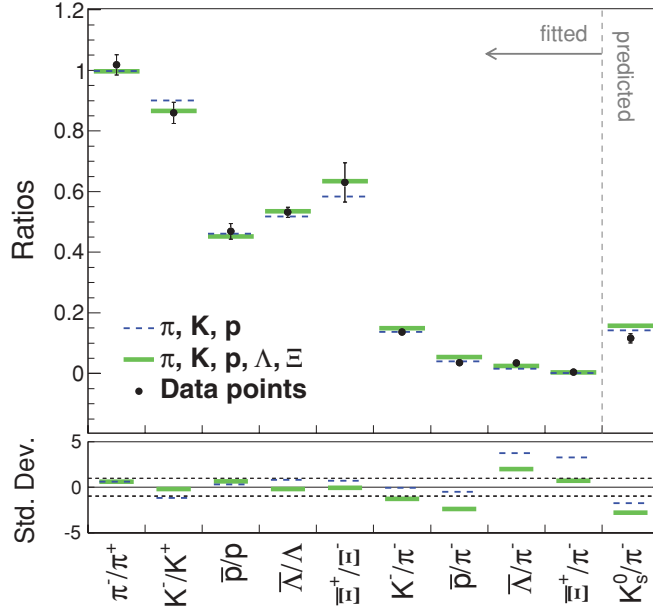
FIG. 9. (Color online) Particle-yield ratios as obtained by measurements (black dots) for the most central (0–5%) Au + Au collisions at 62.4 GeV and statistical model predictions (lines). The ratios indicated by the dashed lines (blue) were obtained by using only π, K, and protons, whereas the ratios indicated by the full lines (green) were obtained by also using the hyperons in the fit.

of γ_s remains constant at 0.88 ± 0.06. The particle ratios, including the strange baryons, are well described by the thermal fit, but it overpredicts the production of $\bar{p}$ with respect to pions.

Figure 10 shows the evolution of the chemical freeze-out temperature [Fig. 10(top)] and the strangeness phase-space occupancy factor [Fig. 10(bottom)] with the number of participants. The solid symbols represent the results for $\sqrt{s_{NN}} = 62.4$ GeV and the open symbols represent the result for $\sqrt{s_{NN}} = 200$ GeV. $T_{\rm ch}$ is independent of the centrality of the collision and its value is consistent with the top RHIC energy measurements. In contrast, γ_s increases from a lower value for peripheral collisions to saturate at a value consistent with unity for the most central events at $\sqrt{s_{NN}} = 200$ GeV and close to unity (0.87 ± 0.07) at $\sqrt{s_{NN}} = 62.4$ GeV. These results are similar to the results obtained previously at the higher RHIC energies, where γ_s rises from peripheral collisions and reaches values consistent with unity for the most central events [32].

Figure 11 shows the energy dependence of the chemical freeze-out temperature and the baryon chemical potential. The open symbols were extracted from Ref. [22]. The solid stars show the values obtained from this analysis for $\sqrt{s_{NN}} = 62.4$ and for the 200-GeV STAR data with the same particle ratios. These results are consistent with other thermal fits presented in Ref. [22] for the same energy range, where data points from other RHIC experiments are considered. The dashed curves in Fig. 11 are the numerical parametrizations of $T_{\rm ch}$ and μ_B presented in Ref. [30] using:

$$\mu_B(\sqrt{s}) = \frac{1.308\,{\rm GeV}}{1 + 0.273\,{\rm GeV}^{-1}\sqrt{s}} \quad (6)$$
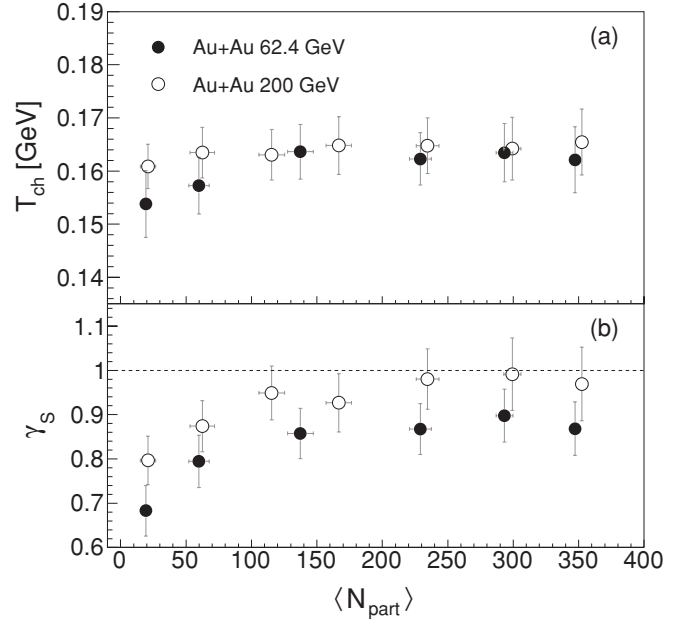

FIG. 10. Chemical freeze-out temperature $T_{\rm ch}$ (a) and strangeness saturation factor γ_s (b) as a function of the mean number of participants.

and

$$T_{\rm ch} = 0.166\,{\rm GeV} - 0.139\,{\rm GeV}^{-2}\mu_B^2 - 0.053\,{\rm GeV}^{-4}\mu_B^4. \quad (7)$$

The values obtained in this analysis for $T_{\rm ch}$ and μ_B from the Au + Au 62.4-GeV data are in good agreement with the parametrizations that were obtained fitting the data points at
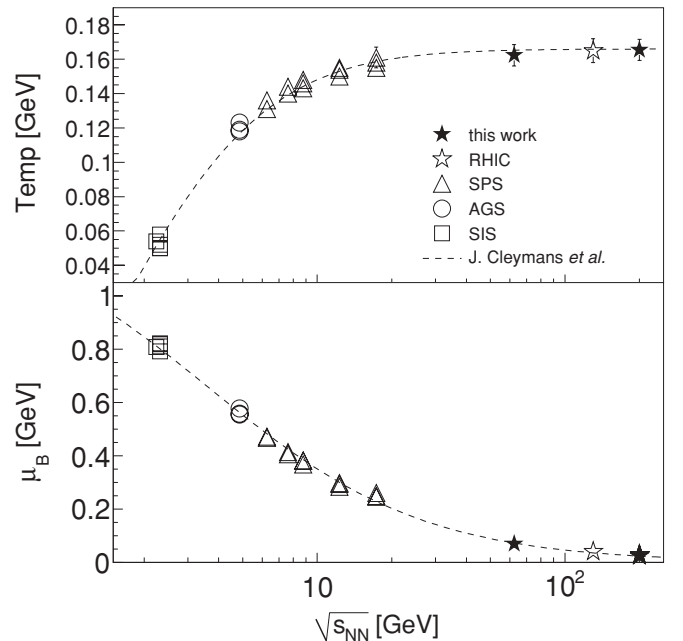

FIG. 11. Temperature and baryon chemical potential obtained from thermal model fits as a function of $\sqrt{s_{NN}}$ (see Ref. [22]). The dashed lines correspond to the parametrizations given in Ref. [22]. The solid stars show the result for $\sqrt{s_{NN}} = 62.4$ and 200 GeV.

higher and lower energies. As the collision energy increases, the baryon chemical potential decreases continuously reaching very small values at RHIC. In contrast, the chemical freeze-out temperature (T_{ch}) seems to achieve saturation at approximately 160 MeV and all three RHIC energy points shown in Fig. 11 are already at this temperature.

B. Strangeness enhancement

Strangeness enhancement is traditionally defined as the ratio of the strange particle yield measured in heavy-ion collisions, normalized by the mean number of participant nucleons ($\langle N_{part} \rangle$) and the yield measured in $p + p$ collisions. Strangeness enhancement was observed at the lower SPS energies [7] as well as at higher RHIC energies [9]. The multistrange baryons show a higher enhancement factor than the Λ particles, which is consistent with the picture of the enhancement of $s\bar{s}$ pair production in a dense partonic medium as opposed to a pure hadronic medium [5]. It is also argued that part of the enhancement can be due to canonical suppression effects in $p + p$ collisions [33]. In this scenario, the production of strange hadrons is actually suppressed in $p + p$ collisions due to limitations of phase space. To discriminate among the different mechanisms that can affect the strangeness enhancement factors, it is necessary to study the systematic behavior for different collision energies, systems, and centralities.

Since there are no data on strange baryon production for $p + p$ collisions at $\sqrt{s_{NN}} = 62.4$ GeV for comparison, we show the ratios of strange baryons and π mesons in Au + Au collisions as a function of dN_{ch}/dy normalized to the ratio in the most peripheral centrality bin (Fig. 12). The Ω data points were not included in this plot due to the difference in centrality selections. The measurements at $\sqrt{s_{NN}} = 62.4$ GeV [Fig. 12(left panels)] and 200 GeV [Fig. 12(right panels)] are shown for strange baryon to pion ratios in the top panels and for antiparticles in the lower panels. The p/π and $\bar{p}/\pi$ ratios have been included for comparison [14].

It is seen that the strange baryon-to-pion ratio increases with centrality and the relative enhancement is higher than observed in the p/π ratio. The multistrange baryon Ξ is the particle with the highest enhancement. In the 62.4-GeV data, there are indications of a difference in the enhancement rate between the strange baryons and antibaryons, with the latter showing a smaller increase with centrality. This difference can be due to the nonzero net-baryon density which makes it easier to form strange baryons than strange antibaryons. In addition, the lower net baryon density at 200 GeV reduces the difference between strange baryons and antibaryons at this energy. At 200 GeV, there is no significant difference between baryon and antibaryon enhancement for all particle species, but the hierarchy of enhancement observed at 64.2 GeV is maintained at the top RHIC energy. From the traditional strangeness enhancement data, where the yields are normalized by the $p + p$ data, the onset of the enhancement is pronounced and is already present in the most peripheral heavy-ion collisions, consistent with the effect that would be expected from the canonical suppression hypothesis. In this context, the increase observed in Fig. 12, which is normalized by the peripheral bin of the measured Au + Au collisions, does not include the
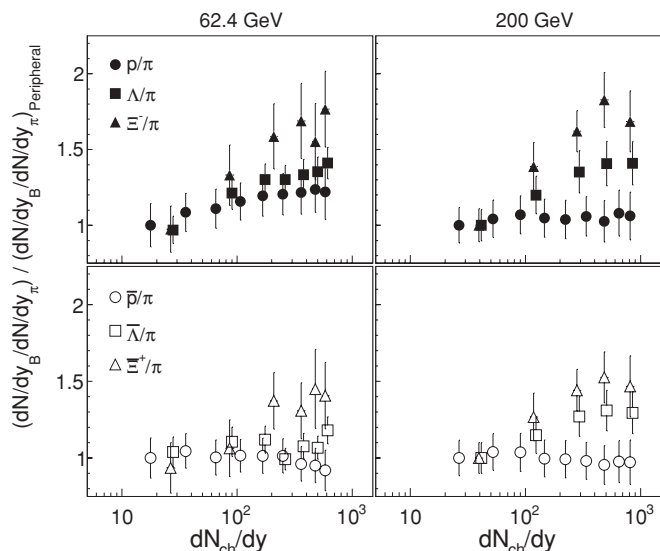

FIG. 12. Ratio of baryon (solid symbols) and antibaryon (open symbols) to π^+ as a function of dN_{ch}/dy for $\sqrt{s_{NN}} = 62.4$ GeV (left) and $\sqrt{s_{NN}} = 200$ GeV (right). The π and p data were extracted from Ref. [14].

effects of the canonical suppression, and could be exclusively due to the enhancement of the $s\bar{s}$ pair production mechanism. However, the p/π ratio also increases with the system size, reflecting the increase of the baryon stopping as the collisions becomes more central. This increase of the net-baryon density would also favor the production of Λ and Ξ with increasing centrality.

Our results show that there is a net increase of the strange baryon production with respect to the pion yields as the system goes from peripheral to central collisions, suggesting a true increase of the $s\bar{s}$ pair production relative to the light quark production in central collisions. This conclusion is further strengthened by the observation of the enhancement in the ϕ/π ratio measured in central Au + Au collisions at 62.4 GeV with respect to peripheral collisions as presented in Refs. [34,35].

Figure 13 shows the ratios of strange baryons to π-meson yields as a function of collision energy. The antibaryon/π-meson ratios increase as a function of energy while the Λ/π and Ξ/π ratios show a decrease from SPS to RHIC energies and then remain constant in the RHIC energy region. The trend in the energy dependence of the Λ/π ratio was already observed in the K^+/π^+ ratio where the peak structure at the SPS energies is more pronounced [14]. This shape is consistent with the net-baryon density dependence on the collision energy [14]. The $\bar{\Lambda}/\pi$ and $\bar{\Xi}^+/\pi$ ratios show a strong monotonic increase with energy. The Ω^-/π and $\bar{\Omega}^+/\pi$ ratios show a smaller increase with energy; however, the experimental uncertainties are large. The dashed lines in this figure correspond to the ratios of these particles using a thermal model calculation with parameters (temperature and chemical potentials) given by the systematic study presented in Ref. [30]. The general trend is well reproduced by this calculation.
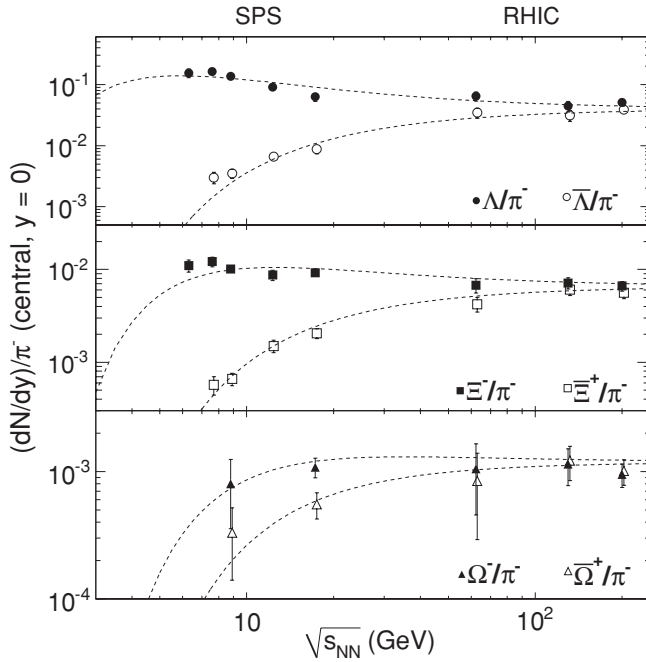
FIG. 13. Ratio of baryon (solid symbols) and antibaryon (open symbols) to π^- as a function of $\sqrt{s_{NN}}$. The lines are the results of the thermal model calculation (see text Sec. IV A). The SPS values are from NA49 [20] (centrality 0–7%) and the RHIC values are from STAR [4,15] (centrality 0–5%). For the multistrange baryons Ξ and Ω (bottom), the SPS results are from NA57 [2] (centrality 0–11%) and the RHIC values are from STAR [15,21] (centrality 0–20%).

C. Nuclear modification factors

One of the most important results from RHIC was the suppression of the particle spectra in the high-p_T region observed via the nuclear modification factor known as R_{AA}. It is the ratio between the measured particle spectra from Au + Au collisions normalized by the corresponding number of binary collisions and the measured spectra in elementary $p + p$ collisions [36]. Together with the measurement of the disappearance of back-to-back high-p_T hadron correlations in central Au + Au collisions attributed to interaction of the energetic jet particles with the formed medium [37], it was concluded that matter created at RHIC is highly interacting. The identified particle R_{AA} from Au + Au collisions at 200 GeV shows that even the strange particle spectra are also suppressed, and there is a grouping of baryons and mesons with respect to their suppression in the intermediate-p_T region. This suppression seems to persist at lower energies and it was observed for pion, proton, and charged kaons in Au + Au collisions at 62.4 GeV [10]. It is important to study whether strange baryons follow the same trend as at 200 GeV and whether the suppression also shows a baryon and meson grouping [37].

For the strange baryons measured at 62.4 GeV it is not possible to evaluate R_{AA} due to the lack of $p + p$ data. However, a comparison between the spectra measured in central collisions and that from the peripheral collisions can also be used to analyze the suppression at high p_T. This comparison is done with the differential nuclear modification factor R_{CP},
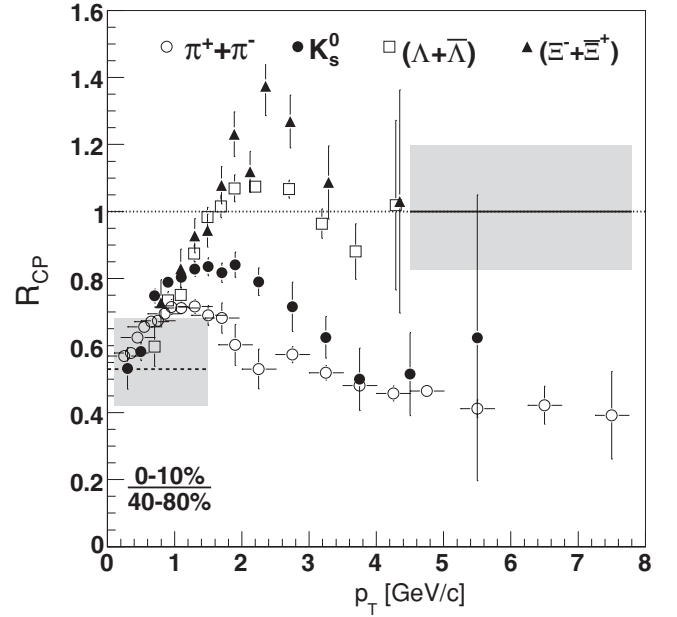

FIG. 14. Nuclear modification factor R_{CP}, calculated as the ratio between 0–10% central spectra and 40–80% peripheral spectra, for π, K_S^0, Λ, and Ξ particles in Au + Au collisions at 62.4 GeV. The π R_{CP} values were extracted from Ref. [10]. The gray band on the right side of the plot shows the uncertainties on the estimation of the number of binary collisions and the gray band on the lower left side indicates the uncertainties on the number of participants.

which is the ratio between the central and peripheral spectra scaled by the number of binary collisions ($\langle N_{\mathrm{bin}} \rangle$):

$$R_{CP} = \left[\frac{d^2 N^{\mathrm{central}}/dp_T dy}{d^2 N^{\mathrm{peripheral}}/dp_T dy} \right] \left[\frac{N_{\mathrm{bin}}^{\mathrm{peripheral}}}{N_{\mathrm{bin}}^{\mathrm{central}}} \right]. \qquad (8)$$

The result of the R_{CP} measurement comparing the spectra of central 0–10% data with the peripheral 40–80% data for the different particle species is shown in Fig. 14. For comparison, the R_{CP} of pions from Au + Au collisions at 62.4 GeV is also included [10].

The K_S^0 data, presented as solid circles show that the R_{CP} reaches a maximum value of approximately 80% at $p_T \approx 2 \, \mathrm{GeV}/c$ and decreases to a ratio of approximately 40% for higher transverse momentum. The general shape of the K_S^0 R_{CP} curve shows the same trend as the π R_{CP} (shown as open circles). In the intermediate-p_T region, between 1.5 and 4 GeV/c, the K_S^0 ratio is higher than the π ratio. The π R_{CP} reaches a maximum around 0.7 at a p_T value of approximately 1.5 GeV/c. But, in the high-p_T region, both K_S^0 and π seem to be equally suppressed, saturating at around 40%. The difference between the K_S^0 and π curves at intermediate p_T is also observed in Au + Au collisions at 200 GeV [38].

The strange baryons, Λ (open squares) and Ξ (solid triangles), show a different behavior. The ratio increases to a maximum above unity at approximately 2.5 GeV/c and then seems to decrease toward unity without showing significant suppression up to 4.5 GeV/c. This behavior differs from that of the proton R_{CP}, which reaches unity at around 2 GeV/c and starts to decrease for higher values of p_T [10].
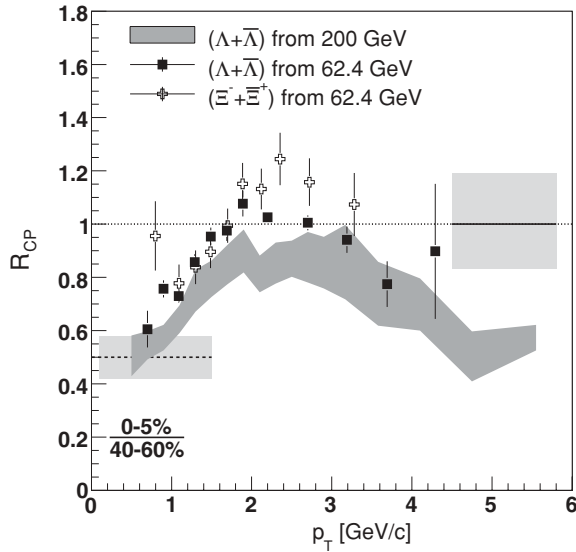
FIG. 15. Nuclear modification factor R_{CP}, calculated as the ratio between 0–5% central spectra and 40–60% peripheral spectra, for Λ and Ξ particles measured in Au + Au collisions at 62.4 GeV. The gray band corresponds to the equivalent R_{CP} curve for the Λ particles measured in Au + Au collisions at 200 GeV [15].

In Fig. 15, the R_{CP} curves of Λ and Ξ measured in Au + Au collisions at 62.4 GeV are compared to the R_{CP} of Λ from Au + Au collisions at 200 GeV presented in Ref. [15]. To allow for a direct comparison to the 200-GeV data, the R_{CP} was calculated from the ratio between spectra of centrality bins 0–5% and 40–60%. The shape of the R_{CP} curve for 200 GeV is similar to the results from 62.4 GeV, also showing a flat region after reaching the maximum, and the onset of suppression only occurs at higher values of p_T. The maximum in the intermediate-p_T region seems to be higher at 62.4 than at 200 GeV. However, considering the systematic uncertainty of the normalization factor, shown as the gray band in the right side of Fig. 15, it is not possible to conclude that the ratio measured at 62.4 GeV is higher than the ratio measured at 200 GeV.

In summary, the K_S^0 spectra at 62.4 GeV are consistent with a suppression scenario for $p_T > 4.0$ GeV/c while the Λ and Ξ baryons seem to show no suppression for $p_T \approx 5$ GeV/c. In Fig. 14 one observes that the difference between the Λ and Ξ curves is smaller than the gap to the K_S^0 data in the intermediate-p_T region, suggesting a baryon-to-meson separation. However, at 62.4 GeV the baryon-meson separation is not as clear as observed in the results from Au + Au collisions at 200 GeV [15].

D. Baryon-to-meson ratio

Another interesting result related to particle spectra and yields obtained from RHIC data is the behavior of the proton-to-pion ratio with p_T, where an anomalous increase of baryon over meson production was observed in the intermediate-p_T region and, furthermore, this increase was higher in more central collisions [39]. This result is referred to as the baryon anomaly, and it is the focus of theoretical discussions
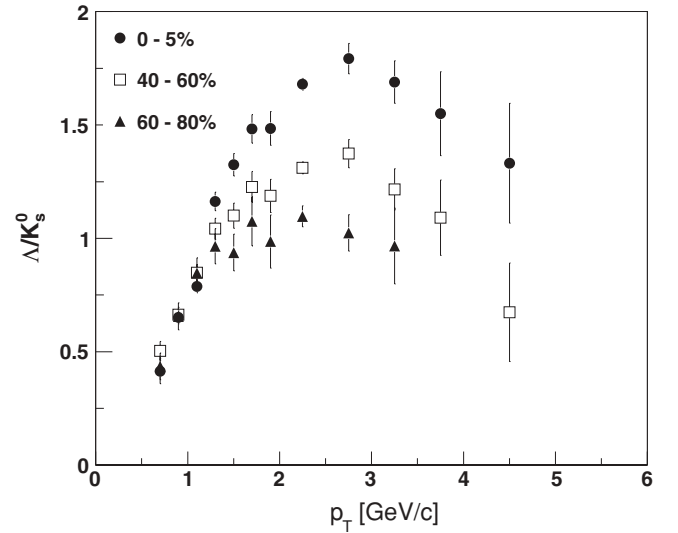

FIG. 16. Λ/K_S^0 ratio as a function of transverse momentum for different centrality classes: 0–5% (solid circles), 40–60% (open squares), and 60–80% (solid triangles) in Au + Au collisions at 62.4 GeV.

that include particle production and also particle interaction with the medium. A baryon-to-meson enhancement was also observed in the strangeness sector, where the ratio Λ over K_S^0 also showed an anomalous increase in the intermediate-p_T region [11].

Figure 16 shows the centrality dependence of the Λ to K_S^0 ratio as a function of p_T. The ratio increases as a function of p_T, reaching a maximum around 2.5 GeV/c. Above this p_T there is a slope change in the curve, and the relative meson production starts to increase with respect to the baryons. In the intermediate-p_T region, between 1.5 and 4 GeV/c, there is a dominance of baryon over meson production. Also, the maximum value of the ratios diminishes when going from central to more peripheral collisions. One of the proposed theoretical explanations for this behavior involves the parton coalescence and recombination mechanisms in hadron production [40–42], where a baryon at a certain p_T results from coalescing partons of a lower p_T. In this scenario, the baryon spectra would have a higher average p_T than mesons, resulting in a ratio that increases with p_T. In general, the coalescence models have been successful in describing the increase of the baryon-to-meson ratio, including the ratio with strange particles.

An alternative proposal comes from the consideration of QCD higher-twist contributions in the initial state of hadron production [43], where baryons would be produced in a color singlet configuration, and thus would be color transparent and not suffer final state interactions, increasing the final yield of baryons over mesons. Within this proposal, the increase of the baryon-to-meson ratio with the increase of centrality would be naturally explained by the higher degree of meson scattering as the volume of the medium increases. In the high-p_T region, the baryon-to-meson ratio starts to decrease with the onset of the contribution from jet fragmentation, in which meson dominates over baryon production.
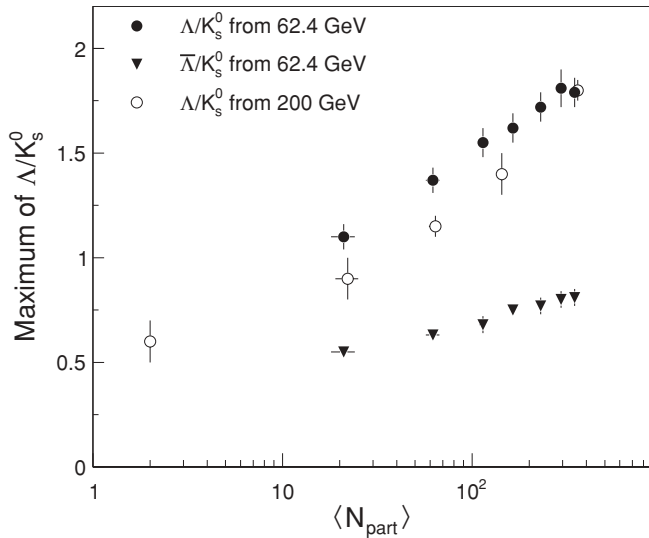
FIG. 17. Maximum value of the Λ/K_S^0 ratio from $Au + Au$ collisions at 62.4 GeV (solid circles) and 200 GeV (open circles) [11] as a function of $\langle N_{part} \rangle$ for different centrality classes. The lowest $\langle N_{part} \rangle$ point corresponds to $p + p$ collisions at 200 GeV [44]. The maximum of the $\overline{\Lambda}/K_S^0$ from $Au + Au$ collisions at 62.4 GeV is shown as solid triangles.

In order to discriminate between different theoretical models it is necessary to study the systematic behavior for different energies and different system size. Figure 17 shows the maximum value of the measured Λ/K_S^0 ratio for the different centrality bins (quantified here by the average number of participants) in $Au + Au$ collisions at 62.4 and 200 GeV [11] as well as $p + p$ at 200 GeV [44]. It is clear that the baryon-to-meson ratio exhibits the same trend at 62.4 GeV as observed at 200 GeV: An increase of the maximum with the increase of the centrality and the same ratio of approximately 1.7 and 1.0 for the most central and peripheral bins, respectively. Figure 17 also shows the $\bar{\Lambda}/K_S^0$ ratio for the 62.4-GeV data. The antibaryon-to-meson ratio peaks at much lower value, below unity, but shows the same trend of increase with centrality. The difference observed between the $\bar{\Lambda}$ and Λ enhancement over the K_S^0 can be attributed to the nonzero net-baryon density.

V. CONCLUSIONS

In this article we present the strangeness production in $Au + Au$ collisions at $\sqrt{s_{NN}} = 62.4$ GeV as measured by the STAR detector at RHIC. For each particle and antiparticle which includes K_S^0, Λ, Ξ, and Ω, the yield and p_T spectra at midrapidity have been extracted for different collision centrality classes from peripheral to the most central events.

Analyzing the antibaryon to baryon ratio of the studied particles as a function of $\sqrt{s_{NN}}$ demonstrates that the

midrapidity baryon-free regime is approached smoothly from the AGS energy to the top RHIC energy. The data at $\sqrt{s_{NN}} = 62.4$ GeV presented here fit well into the systematics of the excitation function of these ratios. Also the production rates of all three antibaryons studied show a smooth increase with energy, whereas the baryon yield excitation functions are susceptible to the interplay between the increase of the pair production mechanism at midrapidity and the decrease of the net-baryon density with increasing rapidity range in higer energy collisions.

The chemical composition of the formed system was studied in the framework of a statistical thermal model, where the strangeness saturation factor parameterizes the degree of equilibration between the strange quarks and the lighter u and d quarks. Results using this model to fit our data show that even for the lower energy 62.4-GeV data, the system created in central $Au + Au$ collisions is still consistent with a saturation of strangeness production, similar to the result obtained at 200 GeV.

Another similarity with the measurements at 200 GeV is seen in the behavior in the intermediate-p_T region. Results of the baryon-to-meson ratio and the nuclear modification factor point to a different behavior of mesons and baryons in this p_T region. Various theoretical proposals were discussed which try to explain these experimental observations. To test any of these models, or even to place tighter constraints on the models, it is necessary to perform a careful and systematic comparison over a wide range of energies. Within this context, the results presented here are a valuable complement to the existing systematics and fill the large gap between the lower energy SPS data and the top RHIC data.

As an overall conclusion, it seems that strangeness production in $Au + Au$ collision at $\sqrt{s_{NN}} = 62.4$ GeV is qualitatively very similar in all aspects to the production at $\sqrt{s_{NN}} = 200$ GeV. All excitation functions vary smoothly from AGS to top RHIC energies.

[1] H. Caines *et al.* (E896 Collaboration), J. Phys. G **27**, 311 (2001).

[2] F. Antinori *et al.* (NA57 Collaboration), Phys. Lett. B **595**, 68 (2004).

[3] C. Alt *et al.* (NA49 Collaboration), Phys. Rev. Lett. **94**, 192301 (2005).

[4] C. Adler *et al.* (STAR Collaboration), Phys. Rev. Lett. **89**, 092301 (2002).

[5] J. Rafelski and B. Muller, Phys. Rev. Lett. **48**, 1066 (1982).

[6] J. Bartke *et al.* (NA35 Collaboration), Z. Phys. C **48**, 191 (1990).

[7] F. Antinori *et al.* (WA97/NA57 Collaboration), Nucl. Phys. A **698**, 118c (2002).

[8] Di Bari D. *et al.* (WA. 85 Collaboration), N. Phys. A **590**, 307 (1995).

[9] B. I. Abelev *et al.* (STAR Collaboration), Phys. Rev. C **77**, 044908 (2008).

[10] B. I. Abelev *et al.* (STAR Collaboration), Phys. Lett. B **655**, 104 (2007).

[11] M. A. C. Lamont, J. Phys. G **30**, S963 (2004).

[12] F. Karsch *et al.*, Nucl. Phys. B, Proc. Suppl. **129**, 614 (2004).

[13] R. V. Gavai and S. Gupta, Phys. Rev. D **71**, 114014 (2005).

[14] B. I. Abelev *et al.* (STAR Collaboration), Phys. Rev. C **79**, 034909 (2009).

[15] J. Adams *et al.* (STAR Collaboration), Phys. Rev. Lett. **98**, 062301 (2007).

[16] K. H. Ackermann *et al.* (STAR. Collaboration), Nucl. Instrum. Methods A **499**, 624 (2003).

[17] M. Shao, O. Barannikova, X. Dong, Y. Fisyak, L. Ruan, P. Sorensen, and Z. Xu, Nucl. Instrum. Methods A **558**, 419 (2006).

[18] F. S. Bieser *et al.*, Nucl. Instrum. Methods A **499**, 766 (2003).

[19] M. L. Miller, K. Reygers, S. J. Sanders, and P. Steinberg, Annu. Rev. Nucl. Part. Sci. **57**, 205 (2007).

[20] T. Anticic *et al.* (NA49 Collaboration), Phys. Rev. Lett. **93**, 022302 (2004).

[21] J. Adams *et al.* (STAR Collaboration), Phys. Rev. Lett. **92**, 182301 (2004).

[22] J. Cleymans, H. Oeschler, K. Redlich, and S. Wheaton, Phys. Rev. C **73**, 034905 (2006).

[23] J. Cleymans, B. Kampfer, and S. Wheaton, Phys. Rev. C **65**, 027901 (2002).

[24] F. Becattini, M. Gazdzicki, A. Keranen, J. Manninen, and R. Stock, Phys. Rev. C **69**, 024905 (2004).

[25] P. Braun-Munzinger, D. Magestro, K. Redlich, and J. Stachel, Phys. Lett. B **518**, 41 (2001).

[26] J. Rafelski, J. Letessier, and G. Torrieri, Phys. Rev. C **72**, 024905 (2005).

[27] N. Xu and M. Kaneta, Nucl. Phys. A **698**, 306 (2002).

[28] J. Takahashi (for the STAR Collaboration), J. Phys. G **36**, 064074 (2009).

[29] P. Braun-Munzinger, I. Heppe, and J. Stachel, Phys. Lett. B **465**, 15 (1999).

[30] J. Cleymans, H. Oeschler, K. Redlich, and S. Wheaton, J. Phys. G **32**, S165 (2006).

[31] S. Wheaton, J. Cleymans, and M. Hauer, Comput. Phys. Commun. **180**, 84 (2009).

[32] J. Takahashi (for the STAR Collaboration), J. Phys. G **35**, 044007 (2008).

[33] A. Tounsi, A. Mischke, and K. Redlich, Nucl. Phys. A **715**, 565 (2003).

[34] B. I. Abelev *et al.* (STAR Collaboration), Phys. Rev. C **79**, 064903 (2009).

[35] B. I. Abelev *et al.* (STAR Collaboration), Phys. Lett. B **673**, 183 (2009).

[36] J. Adams *et al.* (STAR Collaboration), Phys. Rev. Lett. **91**, 172302 (2003).

[37] C. Adler *et al.* (STAR Collaboration), Phys. Rev. Lett. **90**, 082302 (2003).

[38] B. I. Abelev *et al.* (STAR Collaboration), Phys. Rev. Lett. **99**, 112301 (2007).

[39] B. I. Abelev *et al.* (STAR Collaboration), Phys. Rev. Lett. **97**, 152301 (2006).

[40] R. C. Hwa and C. B. Yang, Phys. Rev. C **67**, 034902 (2003).

[41] V. Greco, C. M. Ko, and P. Levai, Phys. Rev. Lett. **90**, 202302 (2003).

[42] R. J. Fries, B. Muller, C. Nonaka, and S. A. Bass, Phys. Rev. C **68**, 044902 (2003).

[43] S. J. Brodsky and A. Sickles, Phys. Lett. B **668**, 111 (2008).

[44] B. I. Abelev *et al.* (STAR Collaboration), Phys. Rev. C **75**, 064901 (2007).